

# An Image Analysis System for Near-infrared (NIR) Fluorescence Lymph Imaging

Jingdan Zhang<sup>a</sup>, Shaohua Kevin Zhou<sup>a</sup>, Xiaoyan Xiang<sup>a\*</sup>  
John C. Rasmussen<sup>b</sup>, and Eva M. Sevick-Muraca<sup>b</sup>

<sup>a</sup>Whole Body Analytics Program, Siemens Corporate Research, Princeton, NJ, USA;

<sup>b</sup>Center for Molecular Imaging, The Brown Foundation Institute of Molecular Medicine,  
University of Texas Health Science Center at Houston, TX, USA

## ABSTRACT

Quantitative analysis of lymphatic function is crucial for understanding the lymphatic system and diagnosing the associated diseases. Recently, a near-infrared (NIR) fluorescence imaging system is developed for real-time imaging lymphatic propulsion<sup>1,2</sup> by intradermal injection of microdose of a NIR fluorophore distal to the lymphatics of interest. However, the previous analysis software<sup>3,4</sup> is underdeveloped, requiring extensive time and effort to analyze a NIR image sequence. In this paper, we develop a number of image processing techniques to automate the data analysis workflow, including an object tracking algorithm to stabilize the subject and remove the motion artifacts, an image representation named flow map to characterize lymphatic flow more reliably, and an automatic algorithm to compute lymph velocity and frequency of propulsion. By integrating all these techniques to a system, the analysis workflow significantly reduces the amount of required user interaction and improves the reliability of the measurement.

**Keywords:** near-infrared fluorescence imaging, lymphatics, lymphatic imaging, lymphatic function, lymphatic function imaging analysis, Hough Transform

## 1. INTRODUCTION

The lymphatic system is a network of capillaries, vessels, and lymph nodes that carry a clear fluid called lymph. It collects excess fluid, cellular debris, proteins, and foreign contaminants from the interstitial space, filters the fluid or lymph, and return it to the venous system. The impairment of lymphatic transport capacity causes fluid and protein accumulation, which in turn leads to lymphedema. Lymphedema is a lifelong condition progressing from swelling and scarring to immune dysregulation and malnutrition. Lymph function is also implicated in diseases of significant prevalence, such as diabetes, obesity, cancer, and asthma. The ability to quantitatively image lymph function is of importance for managing lymphedema or diagnosing the diseases associated with lymphatic system.<sup>5</sup>

Recently, a near-infrared (NIR) fluorescence imaging system is developed for real-time imaging lymphatic propulsion.<sup>1,2</sup> NIR fluorescence imaging of the lymphatics (shown for a human arm in figure 1 (A-C)) is achieved by intradermal injection of microdose of a NIR fluorophore distal to the lymphatics of interest. As the fluorophore is taken up, packets of fluorescent lymph are propelled from the injection sites towards the regional nodal basin via contractile, lymphatic structures called lymphangions. Functional lymphatic vessels are often detected by imaging the transiting of NIR fluorophore packets and in other situations by a dim staining.

In,<sup>3,4</sup> an image analysis system is proposed to quantify lymphatic functions using NIR fluorescence image sequences. When analyzing an image sequence, several regions of interest (ROIs) located along a fluorescent lymphatic vessel are identified manually. For each ROI, a curve of fluorescent intensity as a function of time is plotted by averaging fluorescent intensity within the ROI for every frame of the sequence, as shown in figure 1(D). The curve illustrates the spontaneous propulsive lymphatic flow as indicated by the fluorescence intensity peaks caused by the packets of fluorescent lymph. From the time-of-arrival of packets between ROIs located along a vessel, the lymph velocity and frequency of propulsion can be determined.

---

\*This research was done when Xiaoyan Xiang was an intern at Siemens.

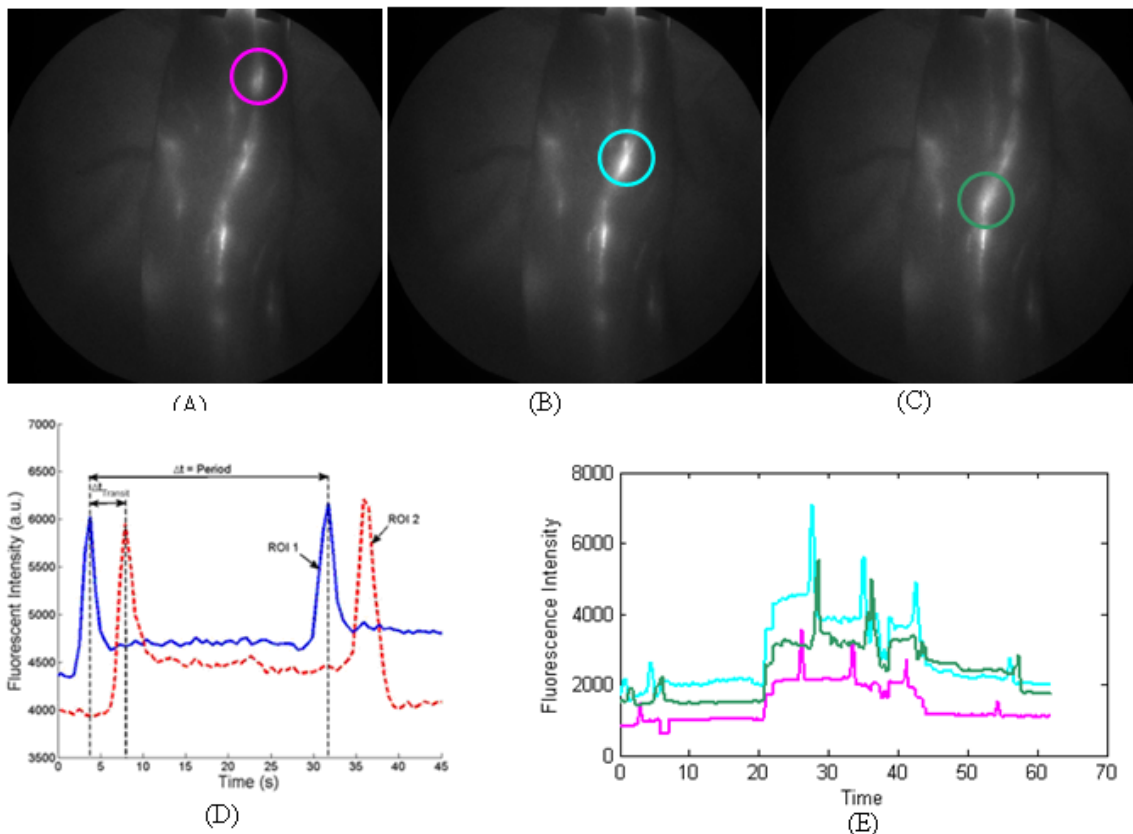


Figure 1. (A-C) Frames from a video of lymphatic flow with the circle in each frame indicating a propelled fluorescent lymph packet on medial side of a human arm. (D) The plot of fluorescent intensity as a function of time at two distinct regions of interest. The lymph velocity and frequency of propulsion can be determined. (E) The curves of fluorescent intensity at three ROIs indicated as circles in (A-C).

Although the above image analysis system is conceptually simple, it suffers several practical issues. First, a fluorescent intensity curve is noisy due to the heavy noise and intensity fluctuation of NIR imaging system. Further, as observed in figure 1(E), the shape of the fluorescent intensity curve is sensitive to the ROI location, which is haphazardly located by user input. As a result, an individual curve cannot provide reliably position measurement of the fluorescent packets. Second, the peaks on a curve are identified manually, which is a time-consuming and tedious task. Third, in an image acquisition procedure, the subject usually has small movement, such as the arm tremble in figure 1(A-C). The movement introduces motion artifacts in the plots that complicate analysis. Because of these issues, extensive time and effort are required to analyze an image sequence.

In this paper, we propose a new system named Automated Lymphatic Function Imaging Analysis (ALFIA) to analyze lymphatic flow in NIR fluorescence image sequences. A variety of image analysis techniques are developed for ALFIA. More specifically, we apply an object tracking algorithm to stabilize the subject and remove the motion artifacts; we propose an image representation named flow map to describe the lymphatic flow more reliably; and we develop an automatic algorithm to compute lymph velocity and frequency of propulsion. By integrating all these techniques to a system, a more reliable measurement is achieved while the labor cost associated with data analysis is greatly decreased.

The remaining of the paper is organized as follows. Section 2 briefs the analysis workflow of ALFIA and elaborates the algorithms developed for ALFIA. Section 3 presents our experimental results. Section 4 concludes the paper.

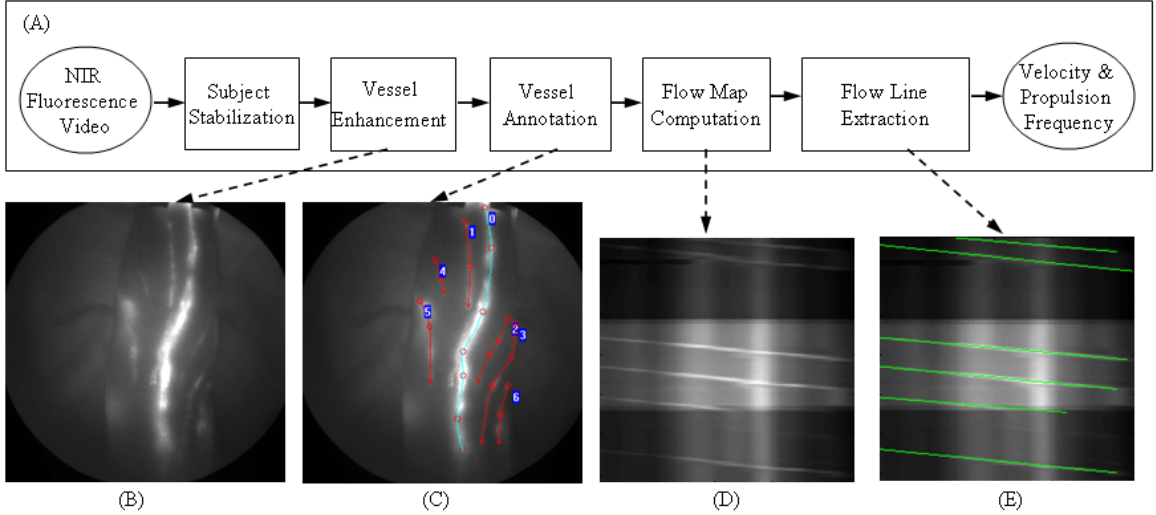


Figure 2. (A) Analysis workflow of ALFIA. (B) Aggregated image. (C) Manual vessel annotation. (D) Flow map. (E) Flow line extraction.

## 2. METHOD AND EXPERIMENT RESULTS

### 2.1 Overview Of analysis workflow

The ALFIA workflow for analyzing lymphatic functions is illustrated in figure 2(A). The input is a near-infrared (NIR) fluorescence video captured by a fixed NIR camera.<sup>2</sup> The output is lymph velocity and frequency of propulsion in each lymphatic vessel.

A subject being imaged usually is not fully stable and has some small movements. The subject stabilization module tracks the movement of the subject in the video to ensure that a position in the image coordinate always correspond to the same anatomic position of the subject across the frames.

After subject stabilization, the vessel enhancement module computes an aggregated image to give better visualization of the lymphatic vessels. As shown in figure 1(A-C), the overall lymphatic vessel structure cannot be clearly identified in one image. Only parts of vessels in which fluorescent lymph packets are passing are highlighted. We create the aggregated image by computing the maximum intensity of each pixel across the whole video. The lymphatic architecture can be identified more reliably in the aggregated image, as shown in figure 2(B).

Then, the vessels are annotated manually by a user in the aggregated image. We use a spline<sup>6</sup> to represent a vessel and the user only needs to annotate several control points. An example of vessel annotation is shown in figure 2(C).

For each annotated vessel, we densely sample points on the vessel and compute a 2D flow map  $M$  across the video.  $M(n, j)$  represents the intensity of the  $n$ th sample point at the  $j$ th frame. It computed as:

$$M(n, j) = \frac{1}{|N(u_n, v_n)|} \sum_{(u, v) \in N(u_n, v_n)} I_j(u, v), \quad (1)$$

where  $(u_n, v_n)$  is the image coordinate of the  $n$ th point;  $N(u_n, v_n)$  defines a small neighborhood around  $(u_n, v_n)$ ; and  $I_j$  is the  $j$ th frame. Compared with the curves used in 1(E), the flow map gives much more reliable trajectories of fluorescent lymph packets, as shown in figure 2(D).

As discussed in,<sup>3</sup> the lymphatic flow can be assumed to have a constant velocity in each propulsion. This assumption can be verified in figure 2(D) as the fluorescent trajectories are straight lines, which are called flow lines. The flow line extraction module automatically detects these lines. An example of detected lines are shown in figure 2(E). Finally, the flow velocity and propulsion frequency are estimated by computing the flow line slopes and the time interval between two consecutive flow lines.

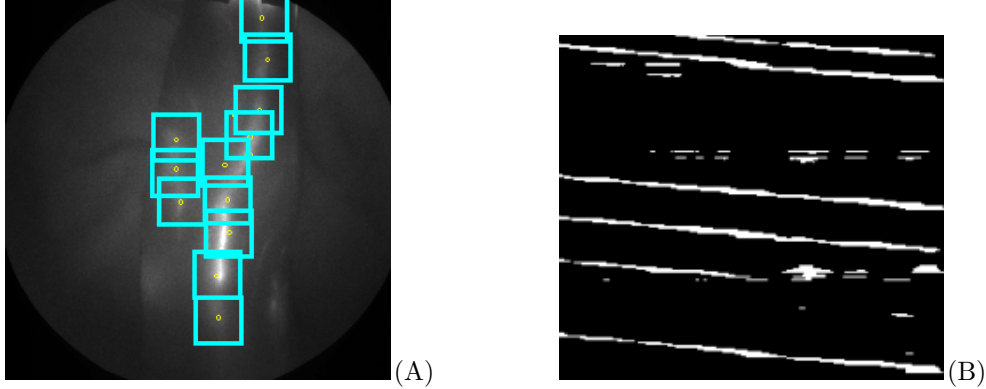


Figure 3. (A) Image patches for representing the appearance of a subject. (B) Binary mask of the flow map in figure 2(D).

## 2.2 Subject stabilization

The goal of subject stabilization is to track the movement of the subject in the video for reducing the motion artifacts. Without subject stabilization, the aggregated image and the flow map will have lower image quality, as shown in figure 5.

Given a image sequence,  $\{I_1, \dots, I_J\}$ , let the reference frame to be  $I_1$  and let the transformation of the subject in  $I_1$  to the subject in the  $j$ th frame  $I_j$  to be  $T_j$ . In our experiments, the transformation is modeled as 2D rigid translation, as the subject is loosely fixed and only small movement is allowed. A large number of tracking algorithms have been proposed in literature.<sup>7</sup> Here we estimate  $T_j$ ,  $j = 2, \dots, J$ , based on image appearance consistency and the smoothness constraint of the subject movement.

The tracking algorithm first identifies a set of salient points  $C = \{c_1, \dots, c_K\}$  belonging to the subject in the reference frame  $I_1$ . In a NIR fluorescence image, the relative high intensity regions belong to the foreground subject, as a high fluorescent intensity value is caused by either fluorescent lymph packets or lymphatic vessels stained by NIR fluorophore. Following this observation, we sparsely sample the salient points from these regions. For image  $I_j$  with subject transformation  $T_j$ , we use a set of image patches  $Q_j = \{q(I_j, T_j(c_1)), \dots, q(I_j, T_j(c_K))\}$  centered at the transformed salient points to represent the image appearance of the subject. An image patch set is shown in figure 3(A).

In tracking, we estimate  $T_j$ ,  $j = 1, \dots, J$ , by minimize an energy function:

$$E(\{T_j\}) = \alpha \sum_{j=2}^J E_I(Q_1, Q_j) + \beta \sum_{j=2}^J E_I(Q_{j-1}, Q_j) + \sum_{j=2}^J E_s(T_{j-1}, T_j), \quad (2)$$

where  $E_I$  measures intensity consistency of the subject between two images,  $E_s(T_{j-1}, T_j)$  is the smoothness constraint between two consecutive frames, and  $\alpha$  and  $\beta$  are weight coefficients. By enforcing the intensity consistency between the reference frame and the tracking frames and between two consecutive frames, we have a most robust consistency measurement for reducing the possibility of drifting. When computing  $E_I$ , due to noise and intensity fluctuation of NIR images, normalized cross-correlation is applied to compute the similarity of each image pair. The energy function 2 can be minimized using Dynamic Programming (DP).<sup>8</sup>

## 2.3 Flow line extraction

Given a flow map, ALFIA automatically extracts the flow lines. As observed in figure 2(D), a flow line has relatively higher intensity than its surrounding regions. Intensity thresholding can be applied to mask out flow-line pixels. However, there are also some regions with high intensity caused by intensity fluctuation of NIR images, leading poor performance of the global thresholding approach. To solve this problem, We apply an adaptive threshold algorithm,<sup>9</sup> which varies the threshold value adaptively based on the relative intensity of local regions. A flow-line mask computed from 2(D) is shown in figure 3(B).

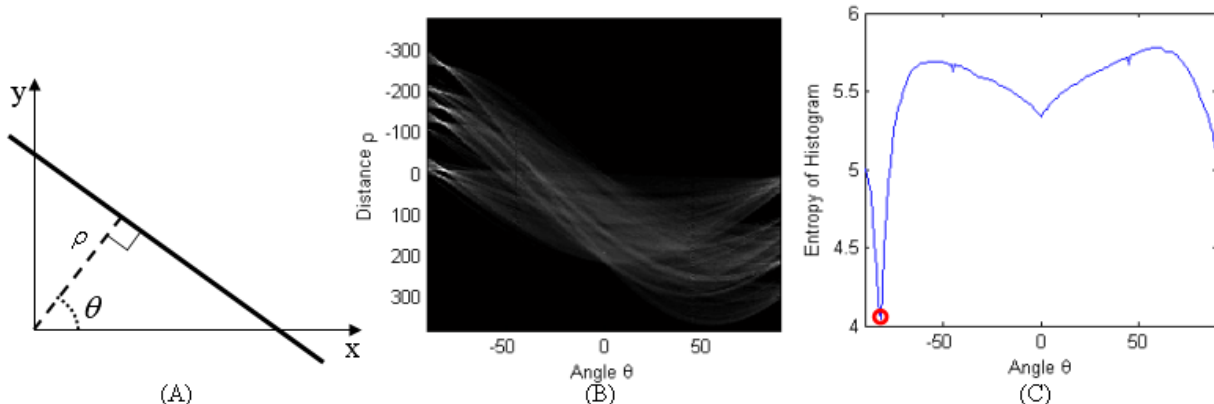


Figure 4. Flow line extraction using Hough Transform. (A) The polar representation of a straight line. (B) Map of Hough transform. (C) Entropy of  $\mathbf{hist}_\theta(\rho)$  for each  $\theta$ . The red dot indicates the angle that has lowest entropy.

Some noise still exists in the flow-line mask. Hough Transform (HT)<sup>10</sup> is applied to robustly extract lines. The HT uses a polar representation of a straight line:

$$\rho = x * \sin(\theta) + y * \cos(\theta), \quad (3)$$

where  $\rho$  is the distance from the origin to the line and  $\theta$  is the angle of the perpendicular projection from the origin to the line, as illustrated in figure 4(A). A HT map computed from 3(B) is shown in figure 4(B).

An observation is that the angles of the flow lines in a map are roughly the same due to similar velocities of fluorescent lymph packets. Thus we first estimate the overall angle of the flow lines. Based on the HT theory, each column of the HT map forms a histogram of  $\rho$ ,  $\mathbf{hist}_\theta(\rho)$ , voted by all mask pixels with the angle  $\theta$ . When  $\theta$  is equal to the overall angle of the flow lines, the histogram  $\mathbf{hist}_\theta(\rho)$  should concentrate to several major peaks and thus should have the lowest entropy.<sup>11</sup> Following this conclusion, we compute the entropy of  $\mathbf{hist}_\theta(\rho)$  for each  $\theta$  as shown in figure 4(C) and select the angle  $\theta_o$  which has the lowest entropy.

After the overall angle is determined, the individual flow lines can be extracted by identifying peaks in  $\mathbf{hist}_{\theta_o}(\rho)$ . Finally, the parameters of individual lines are further refined by using robust regression.<sup>12</sup>

### 3. EXPERIMENT RESULTS

We demonstrate the performance of ALFIA on two NIR fluorescence videos captured by the system described in.<sup>2</sup> Both videos were acquired with 200 millisecond exposure times to capture lymphatic function in the arm of a normal subject. We used a same parameter setting in the image analysis for all experiments.

The first video has 311 frames. Three frames of the video are shown in figure 1(A-C). The computation time for subject stabilization is around 45 seconds on a PC with a Xeon dual core CPU. Figure 5 compares aggregated images and flow maps computed with and without subject stabilization. Comparing with the individual frames in figure 1(A-C), both aggregated images give better visualization of the overall vessel structure. However, the vessels with weak intensity are blurred in the aggregated image computed without subject stabilization. Further, even for the vessel at the medial side of the arm that has strong intensity, the flow map computed without subject stabilization has undesirable artifacts. Figure 3(B), 4, and 2(E) show the computation of flow line for the vessel at the medial side of the arm. Figure 6 shows flow maps computed from two other vessels annotated in figure 2(C) and the corresponding flow line extraction results. Our algorithm successfully picked out the flow lines with subtle image appearance.

The second video has 244 frames, three of which are shown in figure 7(A-C). Figure 7(D) and 7(E) are aggregated images computed without and with subject stabilization. Figure 7(D) has severe motion artifacts due to the movement of the subject. Our tracking algorithm successfully compensated the subject movement, enabling the intensity of the vessels to be correctly aggregated across the frames. The manually annotated vessels

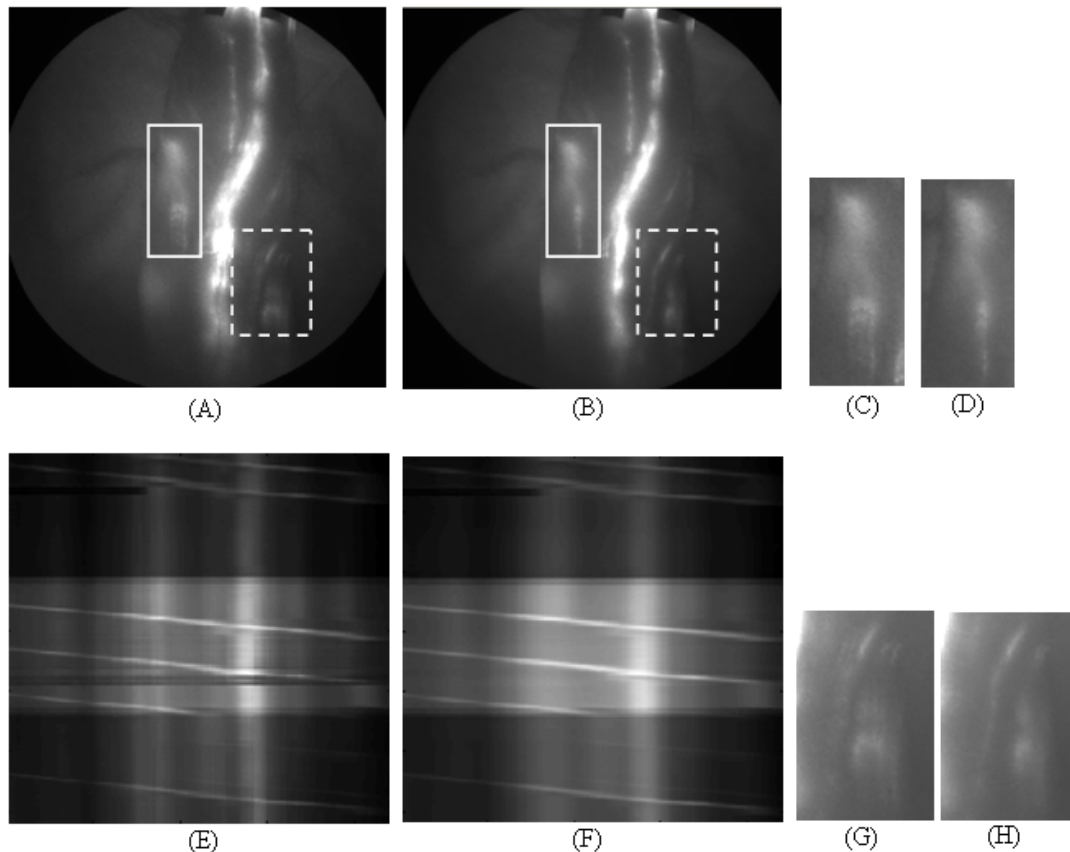


Figure 5. Aggregated images and flow maps computed with (B, D, F, and H) and without (A, C, E, and G) subject stabilization. (A) and (B) are aggregated images. (C), (D), (G), and (H) are enlarged image patches cropped from (A) and (B) respectively to highlight vessels with weak intensity. (E) and (F) are flow maps computed from the long vessel at the medial side of the human arm.

are illustrated in figure 7(F). Figure 8 shows flow maps and flow lines computed from two of the vessels. Note that the flow line extraction algorithm might fail to pick out a flow line if its intensity profile is too weak, such as the flow line at the middle of the image in figure 8(H). As a result, the flow line extraction results need to be verified by users.

#### 4. CONCLUSION

In this paper, we have developed a system named ALFIA for analyzing lymph functions using NIR fluorescence images. In order to reduce the manual labor and improve the reliability of the measurement, we have developed a number of image processing algorithms, including an object tracking algorithm to stabilize the subject, an image representation named flow map to characterize lymphatic flow, and an automatic algorithm to compute lymph velocity and frequency of propulsion. The performance of the system has been demonstrated on real data. The system still requires some user interaction in the analysis workflow, including annotating the lymphatic vessel structure and verifying extracted flow lines. We plan to further reduce the amount of user interaction by automatically detecting vessels and improving the accuracy of the flow line extraction algorithm.

#### REFERENCES

- [1] Sevick-Muraca, E. M., Houston, J. P., and Gurfinkel, M., "Fluorescence-enhanced, near infrared diagnostic imaging with contrast agents," *Curr Opin Chem Biol.* **6**(5), 642–650 (2002).

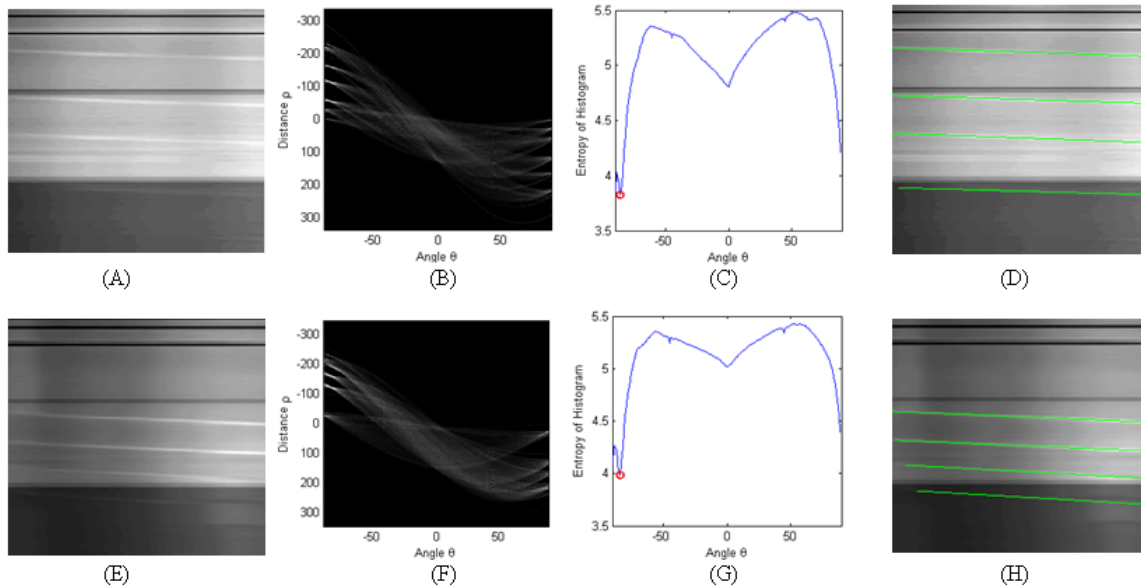


Figure 6. Flow maps and flow line extraction for the first video. (A) and (E) are flow maps computed from two other vessels annotated in figure 2(C). (B) and (F) are Hough Transform maps. (C) and (G) are entropy of  $\mathbf{hist}_\theta(\rho)$  for each  $\theta$ . (D) and (H) are extracted flow lines.

- [2] Sevick-Muraca, E. M. and Rasmussen, J. C., “Molecular imaging with optics: primer and case for near-infrared fluorescence techniques in personalized medicine,” *Journal of Biomedical Optics* **13**(4) (2008).
- [3] Sharma, R., Wang, W., Rasmussen, J. C., Joshi, A., Houston, J. P., Adams, K. E., Cameron, A., Ke, S., Kwon, S., Mawad, M. E., and Sevick-Muraca, E. M., “Quantitative imaging of lymph function,” *Am J Physiol Heart Circ Physiol* **292**(6), 3109–3118 (2007).
- [4] Kwon, S. and Sevick-Muraca, E. M., “Noninvasive quantitative imaging of lymph function in mice,” *Lymphatic Research And Biology* **5**(4), 219–231 (2007).
- [5] Sevick-Muraca, E. M., Sharma, R., Rasmussen, J. C., Marshall, M. V., Wendt, J. A., Pham, H. Q., Bonefas, E., Houston, J. P., Sampath, L., Adams, K. E., Blanchard, D. K., Fisher, R. E., Chiang, S. B., Elledge, R., and Mawad, M. E., “Imaging of lymph flow in breast cancer patients after microdose administration of a near-infrared fluorophore: Feasibility study,” *Radiology* **246**(3), 734–741 (2008).
- [6] Bartels, R. H., Beatty, J. C., and Barsky, B. A., [*An introduction to splines for use in computer graphics and geometric modeling*], Morgan Kaufmann Publishers Inc. (1987).
- [7] Yilmaz, A., Javed, O., and Shah, M., “Object tracking: A survey,” *ACM Comput. Surv.* **38**(4) (2006).
- [8] Bellman, R. E., [*Applied Dynamic Programming*], Princeton Univ. Press (1962).
- [9] Wellner, P., “Adaptive thresholding for the digitaldesk,” *Rank Xerox Technical Report EPC-1993-110* (1993).
- [10] Duda, R. O. and Hart, P. E., “Use of the hough transformation to detect lines and curves in pictures,” *Comm. ACM* **15**, 11–15 (1972).
- [11] Jaynes, E. T., “Information theory and statistical mechanics,” *Physical Review* **106**(4), 620–630 (1957).
- [12] Holland, P. W. and Welsch, R. E., “Robust regression using iteratively reweighted least-squares,” *Communications in Statistics: Theory and Methods* **A6**, 813–827 (1977).

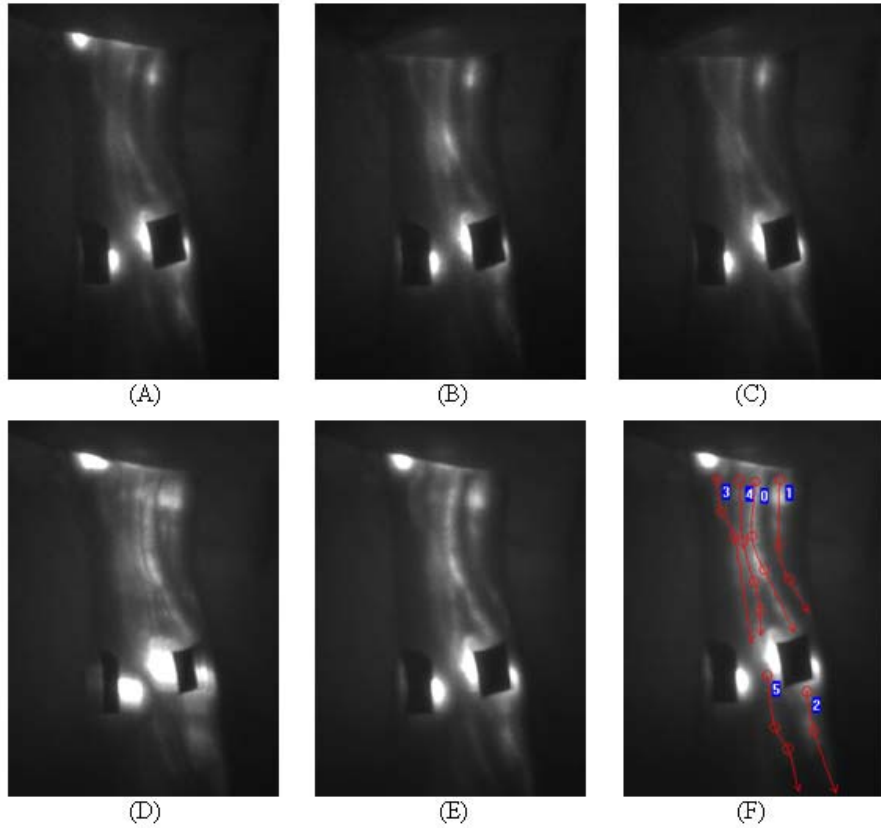


Figure 7. (A-C) Three frames in the second video. (D) Aggregated image computed without subject stabilization. (E) Aggregated image computed with subject stabilization. (F) Vessel annotation.

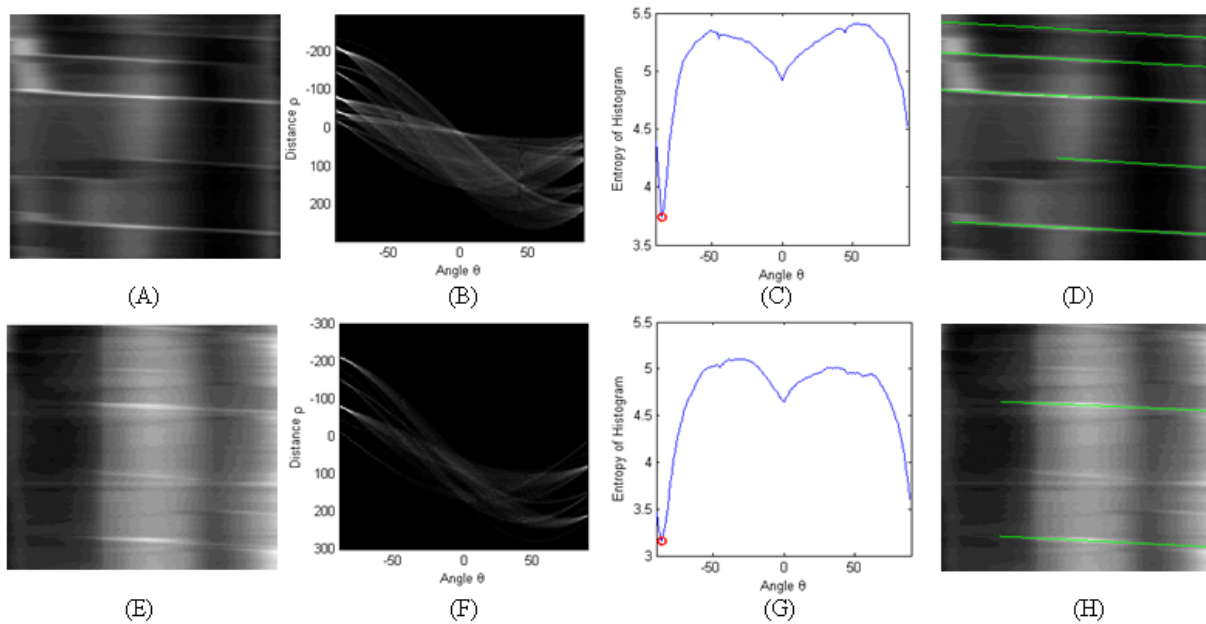


Figure 8. Flow maps and flow line extraction for the second video. (A) and (E) are flow maps computed from two vessels annotated in figure 7(F). (B) and (F) are Hough Transform maps. (C) and (G) are entropy of  $\text{hist}_\theta(\rho)$  for each  $\theta$ . (D) and (H) are extracted flow lines.